

A traveling-wave ultrasonic motor utilizing a ring-shaped alumina/PZT vibrator

Jiang Wu^{1,2,3,4} , Yosuke Mizuno³  and Kentaro Nakamura^{3,4} 

¹State Key Laboratory for Reliability and Intelligence of Electrical Equipment, Hebei University of Technology, Tianjin 300130, People's Republic of China

²Hebei Key Laboratory of Robot Perception and Human-robot Interaction, Hebei University of Technology, Tianjin 300130, People's Republic of China

³Laboratory for Future Interdisciplinary Research of Science and Technology, Tokyo Institute of Technology, Yokohama 226-8503, Japan

E-mail: wujiang@sonic.pi.titech.ac.jp and knakamur@sonic.pi.titech.ac.jp

Received 29 May 2019, revised 25 August 2019

Accepted for publication 14 October 2019

Published 8 November 2019



CrossMark

Abstract

Considering that high Young's moduli and low ultrasonic attenuation of fine ceramics may enhance driving force and reduce energy dissipation, in this study, we exploit the usage of fine ceramics as vibrating bodies of ultrasonic motors. Several alumina vibrating bodies were fabricated and bonded to annular lead-zirconate-titanate (PZT) disks to form ring-shaped vibrators, where traveling waves with the 3rd bending modes were excited to frictionally drive the rotor. First, we explored the fundamental vibration properties. As predicted, the alumina/PZT vibrators provided relatively high force factors, high electromechanical coupling factors, and low damping compared to the stainless-steel/PZT one with similar structure. Subsequently, through experimental assessment on load characteristics, we found that the rotation speed of the alumina/PZT motor at 20 V was larger than that of the stainless-steel/PZT motor at 250 V, and meanwhile, it exhibited superior maximal-torque-to-voltage and maximal-output-power-to-voltage ratios; these results imply that satisfactory performance is achievable with our motor. Besides, alumina's chemical resistance and electrical resistance make our motor potentially applicable to the acid/alkaline atmosphere and the intensively alternating-current magnetic field.

Keywords: ultrasonic motors, alumina, high young's modulus, low ultrasonic attenuation

(Some figures may appear in colour only in the online journal)

1. Introduction

Since ultrasonic motors (USMs) offer the capability to provide quick response, simple structure, and absence of electromagnetic radiation [1–5], they have achieved practical application to several fields [6–9], e.g. auto-focusing system in digital cameras [1]. Vibrators and rotors are the main components of USMs [1, 8] and vibrators basically consist of vibrating bodies (commonly made of metals) and piezoelectric materials [typically, lead zirconate titanate (PZT)] [1, 5, 7, 8]. After preliminarily investigating how vibrating bodies' material constants affected USMs' vibration properties in former studies [4, 10–12], we predicted that high

Young's moduli and low ultrasonic attenuation, which contributed to enhancing the driving force and suppressing energy dissipation [1, 4, 8, 12], were desirable for vibrating bodies [10–12].

In previous studies [1, 8, 13–18], fine-ceramic layers were generally coated onto metal-based vibrators' and/or rotors' surfaces to improve USMs' frictional and abrasional characteristics, but they were too thin to affect vibration properties [1, 8]. To date, there has been almost no report about fine-ceramic-based USMs except Aoyagi *et al*'s motor [19]: a thin PZT film was printed onto a fine ceramic plate to suppress thermally-induced stress in the poling process, but its vibration properties were roughly studied and the load characteristics were completely not explored [19]. Besides, this motor is seemingly incapable of working even when a

⁴ Authors to whom any correspondence should be addressed.

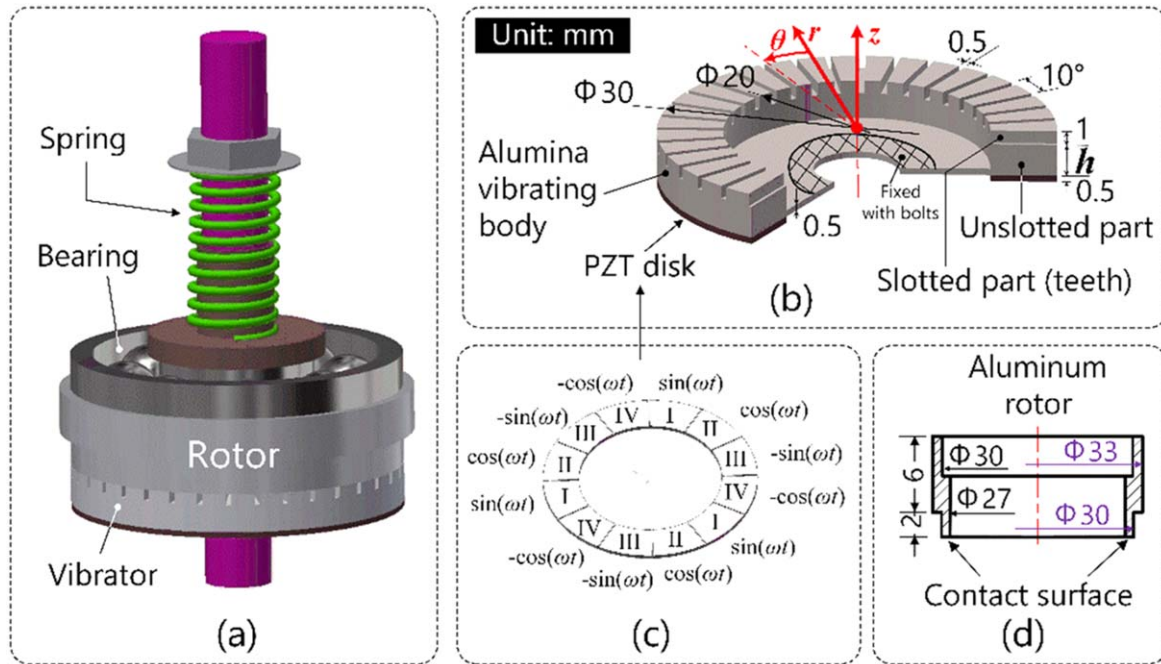


Figure 1. (a) Configuration of the tested alumina/PZT motor; (b) the ring-shaped vibrator, consisting of an alumina vibrating body and (c) an annular PZT disk; and (d) the rotor.

small preload is applied because its PZT film is too thin to generate sufficient vibration amplitude [19]. Thus, it would be meaningful to design new fine-ceramic/PZT motors to examine the actuating capability.

In this study, we fabricated a ring-shaped alumina/PZT vibrator to form a traveling-wave USM and systematically investigated its vibration properties and load characteristics. Here, alumina is employed owing to its relatively low ultrasonic attenuation among commonly-used fine ceramics [12]. Additionally, the ring shape, which has been widely studied in the development of USMs [4, 10, 20–25], is selected as its small profile and hollow structure are attractive advantages for practical usage [1, 8].

2. Configuration

Figure 1(a) schematically illustrates the developed motor, dominantly composed by a vibrator and a rotor. As depicted in figure 1(b), the vibrator incorporates an alumina vibrating body (A995, NTK Ceratec, Sendai, Japan) and an annular PZT disk (C213, Fuji Ceramics, Fujinomiya, Japan). The alumina product has the Young's modulus, bulk density, Poisson's ratio, and purity of 380 GPa, $3.9 \times 10^3 \text{ kg m}^{-3}$, 0.24, and 99.5% [26], respectively. It consists of a back disk 0.5 mm in thickness and a cylindrical part 30 and 20 mm in outer and inner diameters, respectively. Average roughness of the driving surface is $0.12 \mu\text{m}$ [27], far lower than the vibration amplitude [$\sim 7 \mu\text{m}$ (see the following section)]. Some 1 mm deep 0.5 mm wide slots were created on the cylindrical part with 10° intervals. Here, several vibrators with varying un-slotted part's thickness h were prepared to

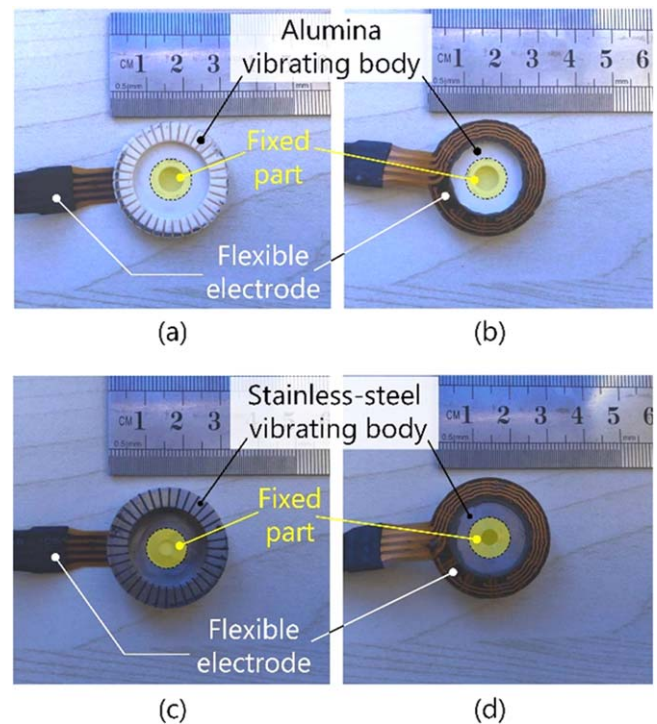


Figure 2. Photos of the alumina/PZT vibrator prototype taken from the (a) top and (b) bottom views and those of the stainless-steel/PZT vibrator prototype taken from the (c) top and (d) bottom views. Note that, though the central holes on bottom disks have different diameters, they should exhibit little effect on the vibration properties as the fixed parts (in yellow) have the same diameters.

explore how the h affects vibration properties. A central hole was introduced on the back disk to fix the vibrator. A polar coordinate system (z , θ , and r axes) is established on the upper

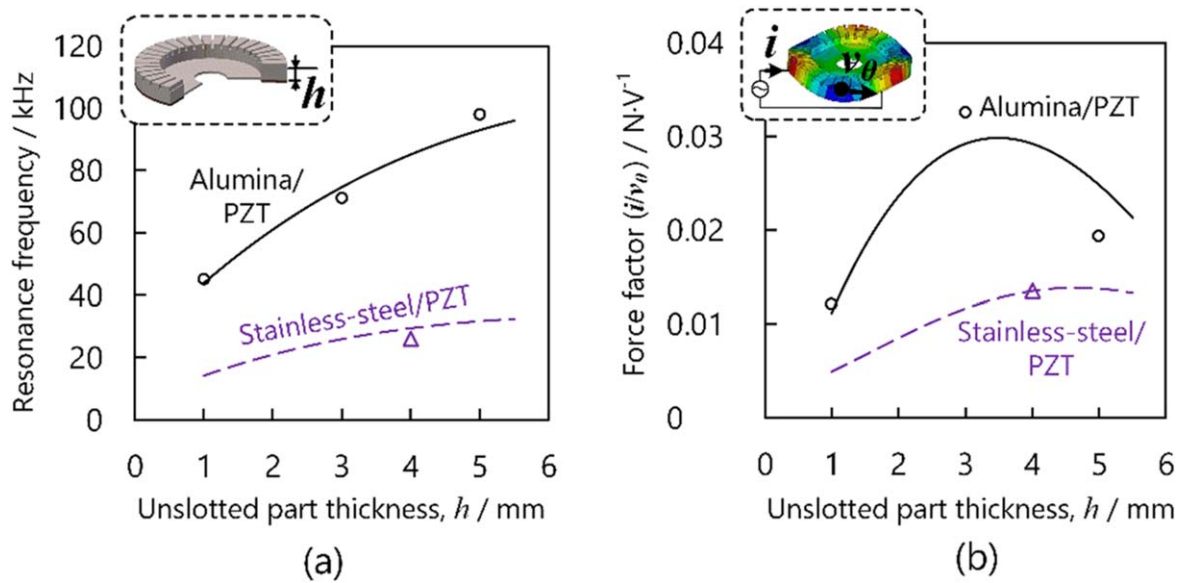


Figure 3. (a) Resonance frequency and (b) force factor of the alumina/PZT vibrators with varying unslotted-part thickness. The solid lines and circles are simulated and experimental results of the alumina/PZT vibrators, respectively. The dashed lines and triangles are the values of the stainless-steel/PZT vibrator.

surface. As shown in figure 1(c), the PZT disk has an outer diameter of 30 mm, an inner diameter of 20 mm, and a thickness of 0.5 mm. One side of the silver electrode was evenly divided into 12 parts with identical polarization directions. The undivided side was bonded to the back surface of the alumina vibrating body with epoxy resin. When alternating voltages with phases, i.e. $U_0\cos(\omega t)$, $-U_0\cos(\omega t)$, $U_0\sin(\omega t)$, and $-U_0\sin(\omega t)$, where U_0 , ω , and t are respectively voltage, angular working frequency, and time, are applied; the 3rd bending mode is excited on the vibrator. Since the sum of these four voltages is zero, electrical potential of the undivided part should be equal to zero [1, 4, 12] and as a consequence, it is not required to connect this side to the ground [1]. The aluminum rotor shown in figure 1(d) has two parts with different diameters. A bearing is inserted into the part with a 33 mm outer diameter, while the bottom surface of the other part is in contact with the outer edge of the vibrator. A spring is used to apply preloads to the rotor to generate frictional force.

Figures 2(a) and (b) illustrate the photos of an alumina/PZT vibrator taken from the top and bottom views, respectively. Instead of feeding lines, a flexible electrode (purchased from Nihon Membrane, Tokyo, Japan) was bonded to the PZT disk's divided side with the non-conductive epoxy-resin adhesive. Here, the applied pressure during thermal solidification and the adhesive's volume were adjusted to achieve both sufficient bonding strength and electrical connection. As shown in figures 2(c) and (d), a stainless-steel (SUS304)/PZT motor was fabricated for performance comparison. Its structure is almost the same as the alumina/PZT ones (see figure 1(b)) except the 4 mm thick unslotted part; the reason for choosing this thickness is explained in the following section.

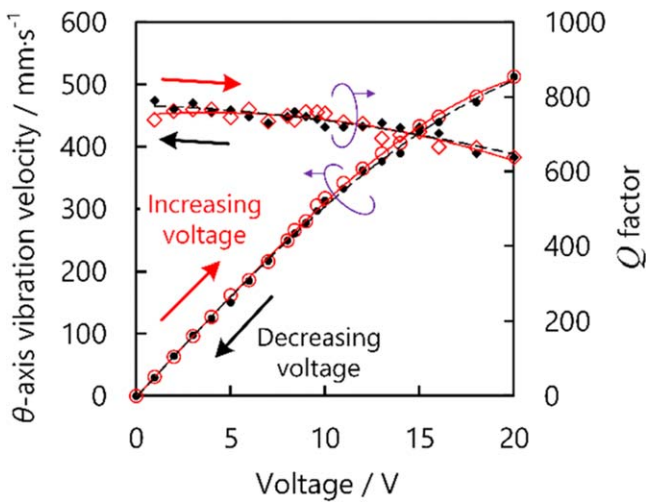
3. Vibration properties

First, we calculated resonance frequencies and force factors of the alumina/and stainless-steel/PZT motors through finite element analysis (FEA) [software: ANSYS (ver. 16.0, ANSYS Inc. Canonsburg, USA)]. Here, the force factor A is defined as the ratio of the current (measured with a current probe: P6021, Tektronix, Beaverton, USA) to the θ -axis vibration velocity (measured with an in-plane vibrometer: IPV100, Polytec, Waldbronn, Germany) [1, 4, 11, 12]. Figure 3(a) shows that the resonance frequencies monotonically increase as the vibrators become thicker. Owing to high stiffness [11], the alumina/PZT vibrator exhibits relatively high resonance frequencies compared to the stainless-steel/PZT one. Figure 3(b) demonstrates that the force factors reach peak values when the alumina/and stainless-steel/PZT vibrators have 3 and 4 mm thick unslotted parts, respectively. Moreover, the maximal force factor is 2.4 times higher for the alumina/PZT than for the stainless-steel/PZT vibrator dominantly owing to alumina's high Young's modulus [12]. Our previous studies [11, 28] have proved that, among the stainless-steel/PZT motors in disk shape (as shown in figures 2(c) and (d)), the one with a large force factor tends to exhibit high performance. On the basis of this knowledge, only the one with a 4 mm thick unslotted part was prepared in this study. Whereas alumina/PZT motors with varying thickness were fabricated to test whether they had the same tendency.

Subsequently, we investigated the vibration properties based on the equivalent circuit model [1]. The motional admittance Y_{m0} , resonance frequency f_r , anti-resonance frequency f_a , and bandwidth corresponding to 0.707 times of the peak amplitude Δf , were initially measured with an impedance analyzer (4294A, Agilent, Santa Clara, CA, USA).

Table 1. Equivalent circuit parameters of alumina/PZT and stainless-steel/PZT vibrators.

Unslotted part thickness (h)/mm	Alumina/PZT			Stainless-steel/PZT
	1	3	5	4
Resonance frequency (f_r)/kHz	49.567	71.225	98.126	26.124
Anti-resonance frequency (f_a)/kHz	49.658	72.073	98.889	26.155
Electromechanical coupling factor (k)	6.1%	15.3%	10.7%	4.9%
Force factor (A)/N V ⁻¹	0.012	0.033	0.019	0.014
Q factor	880	769	775	379
Equivalent damper (γ_m)/N s m ⁻¹	0.624	0.516	0.645	2.089
Equivalent stiffness (s_m)/10 ⁶ N m ⁻¹	171	177	308	130
Equivalent mass (m_m)/10 ⁻³ kg	1.76	0.90	0.81	4.82

**Figure 4.** Variation of the θ -axis vibration velocity as functions of applied voltage (0–20 V).

Then, the electromechanical coupling factor k , mechanical quality factor Q , equivalent damping γ_m , equivalent stiffness s_m , and equivalent mass m_m are calculated with the following equations [1, 18]:

$$k = \sqrt{1 - \left(\frac{f_r}{f_a}\right)^2}, \quad (1)$$

$$Q = \frac{f_r}{\Delta f}, \quad (2)$$

$$\gamma_m = \frac{A^2}{Y_{m0}}, \quad (3)$$

$$s_m = \frac{2\pi f_r \cdot Q \cdot A^2}{Y_{m0}}, \quad (4)$$

and

$$m_m = \frac{Q \cdot A^2}{2\pi f_r \cdot Y_{m0}}, \quad (5)$$

respectively. As table 1 shows, the alumina/PZT vibrator with a 3 mm thick unslotted part (h3 vibrator) exhibits a relatively high electromechanical coupling factor compared to the h1 and h5 vibrators as well as the stainless-steel/PZT one

[12]. In the meantime, the alumina/PZT vibrators exhibit higher Q factors, resulting in lower equivalent damping [1, 4, 8]. Besides, they possess relatively high equivalent stiffnesses and low equivalent masses, which are assumed to originate from the relatively high Young's modulus and moderate density of alumina, respectively [1, 4, 11, 12].

Finally, we explored how the vibration velocity and the Q factor depended on the voltage applied to the h3 vibrator. As figure 4 showed, the vibration velocity linearly increased from 0 to 512 mm s⁻¹. In the meantime, the Q factor exhibited almost no variation as the voltage increased from 0 to 10 V, but a reduction in the voltage range from 10 to 20 V as a consequence of PZT's nonlinearity. Besides, no hysteresis was observed in the vibration-velocity and Q -factor dependences on voltage.

4. Motor performance

4.1. Experimental setup

In this section, we measured load characteristics of the alumina/PZT motors and made comparison with the stainless-steel/PZT one. Figure 5(a) depicts the experimental setup. First, two signals with a 90° phase shift were amplified with bipolar power amplifiers (HSA4051, NF Corp., Yokohama, Japan). Then, inverted signals were created with center-tapped transformers. Two high-frequency power meters (3335, Hioki E. E. Corp., Nagano, Japan) were arranged between the amplifiers and the transformers to measure the electrical input power. Figure 5(b) schematically illustrates the system for evaluating the load characteristics. The torque was measured by pulling up a weight while the rotation speed was estimated with a self-made rotation meter. The mechanical output power equals the product of the torque and the rotation speed.

4.2. Load characteristics

Figure 6 illustrates the variation in the no-load rotation speed of the h3 motor against the phase at the voltage, frequency, and preload of respectively 10 V, 71.2 kHz, and 3.3 N. When the phases were -90° and 100°, the motor provides maximal rotation speeds in clockwise and counterclockwise directions, respectively. Figures 7(a)–(c) respectively plot how the

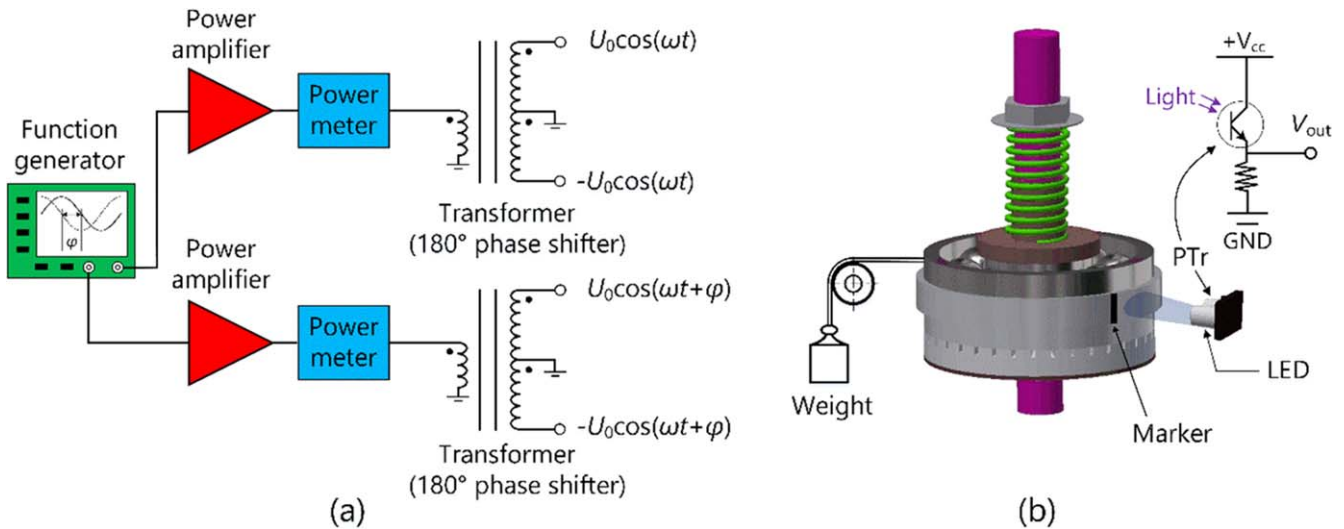


Figure 5. Schematics of (a) the electrical system for applying voltage and (b) the mechanical system for measuring the load characteristics.

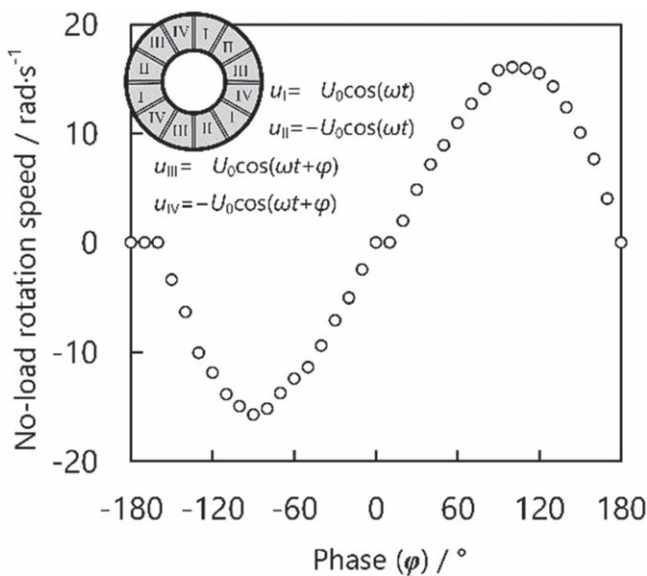


Figure 6. Variation in no-load rotation speed of alumina/PZT motor against phase.

rotation speed, output power, and efficiency change with varying torque. The voltage, working frequency, and phase were set to 10 V, 71.2 kHz, and 100°, respectively. At 3.3 N, the maximal torque, output power, and efficiency reached 12.8 mN m, 58.2 mW, and 6.8%, respectively. When the preload increased to 6.3 N, there existed a reduction in mechanical output as a consequence of lowered efficiency.

Figures 8(a)–(d) respectively demonstrate how the maximal torque, no-load rotation speed, maximal output power, and maximal efficiency of the h3 motor depend on the voltage under different preloads. Every time the voltage and/or preload were varied, the working frequency was adjusted to enable the vibrator to provide maximal vibration velocity. There initially existed a dead region at <2 V [2]. Then, the torques corresponding to the preloads of 2.4 and 3.3 N

became higher as the voltage increased from 5 to 10 V, and approached the saturated value at 10 V [2, 11]. At 6.3 N, the maximal torque (25.9 mN m) was limited by the voltage rather than the preload [2]. The no-load rotation speed increased as the voltage became higher. The maximal output power reached 141 mW. When the voltage and preload were respectively 20 V and 3.3 N, the h3 motor exhibited the maximal efficiency (~8%).

Figures 9(a)–(d) plot the maximal torque, maximal no-load speed, maximal output power, and maximal efficiency of the alumina/PZT motors against their unslotted part thickness, respectively. To avoid their failure (see appendix A), the voltage was set to 20 V. Similar to stainless-steel/PZT ones, the h3 motor exhibits the maximal torque owing to the relatively high force factor [1, 2, 4, 12]. No-load speed is dominantly affected by the θ -axis vibration velocity [2, 11]. The maximal output power achievable with the h3 motor is higher as a consequence of its larger electromechanical coupling factor [4, 18]. The maximal efficiency does not show obvious difference among the alumina/PZT motors as their friction materials are identical [1, 14].

4.3. Performance comparison

Table 2 compared the performance between the h3 motor and the stainless-steel/PZT one. The h3 motor operates in the high vibration region even when the voltage is as low as 20 V. Whereas, at the same voltage, the stainless-steel/PZT motor works in the low vibration region and provides inferior performance. At 250 V, larger preload can be applied to the stainless-steel/PZT vibrator as it stores higher vibration energy [4]. Meanwhile, the frictional coefficient between stainless steel and aluminum (~0.35) is higher than that between alumina and aluminum (~0.25) [29]. Both of them cause relatively high torque of the stainless-steel/PZT motor at 250 V. However, the maximal-torque-to-voltage (T-to-U) ratio of the alumina/PZT motor is 6.9 times the value of the

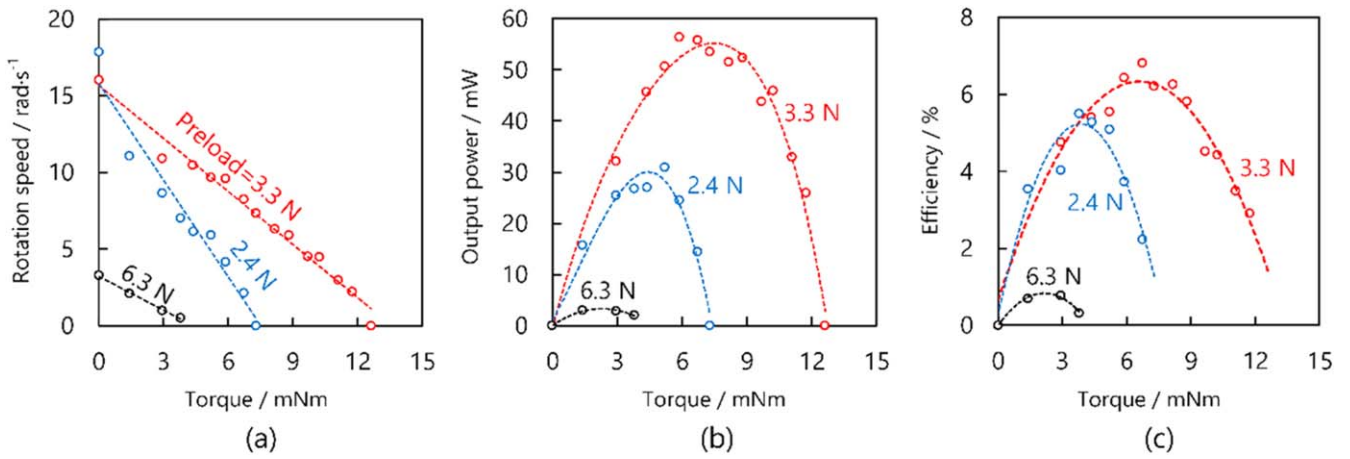


Figure 7. Load characteristics of the h3 motor at 10 V. (a) Rotation speed, (b) output power, and (c) efficiency as functions of torque.

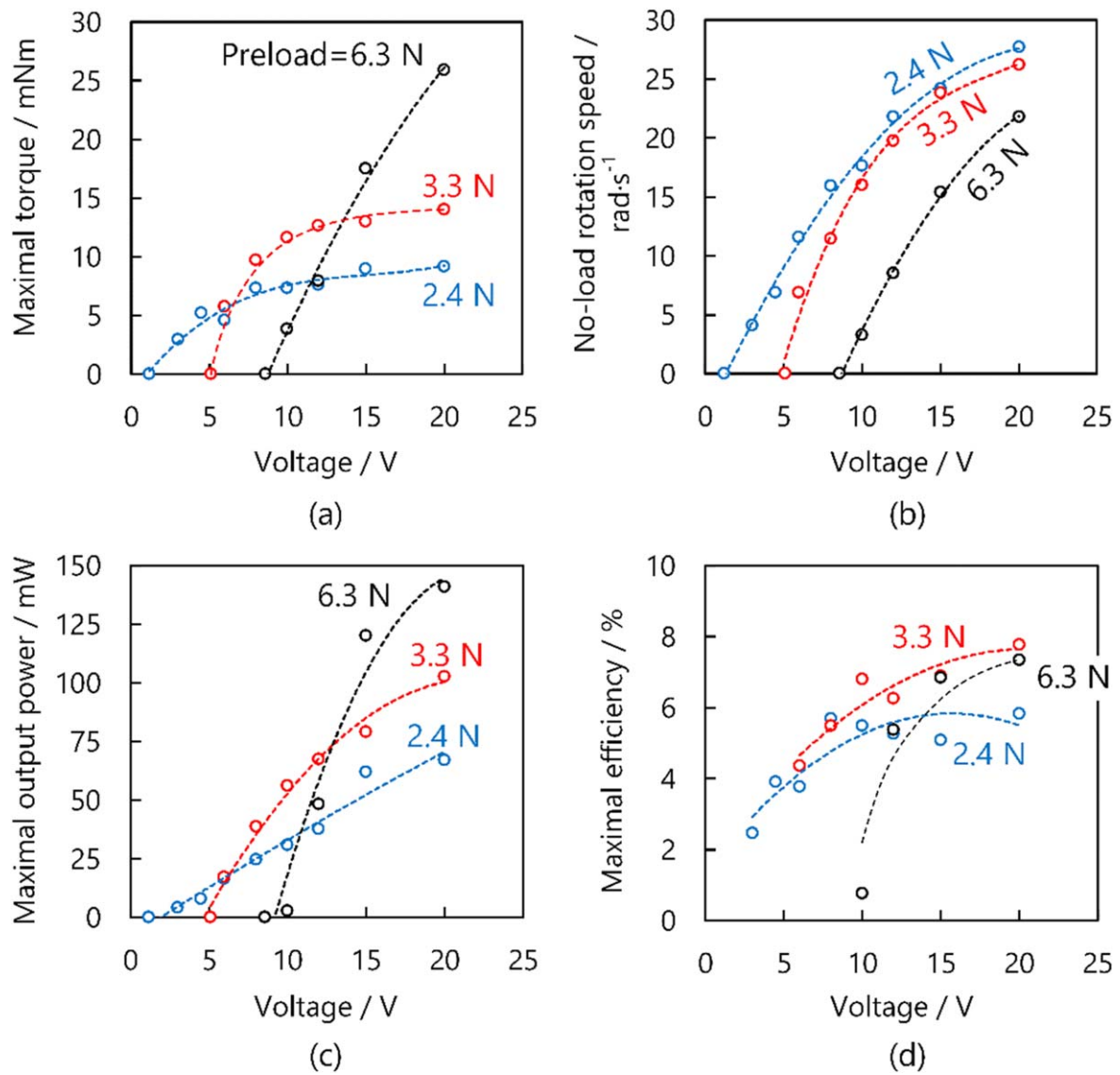


Figure 8. Variations in (a) maximal torque, (b) no-load speed, (c) maximal power, and (d) maximal efficiency of the h3 motor against applied voltage.

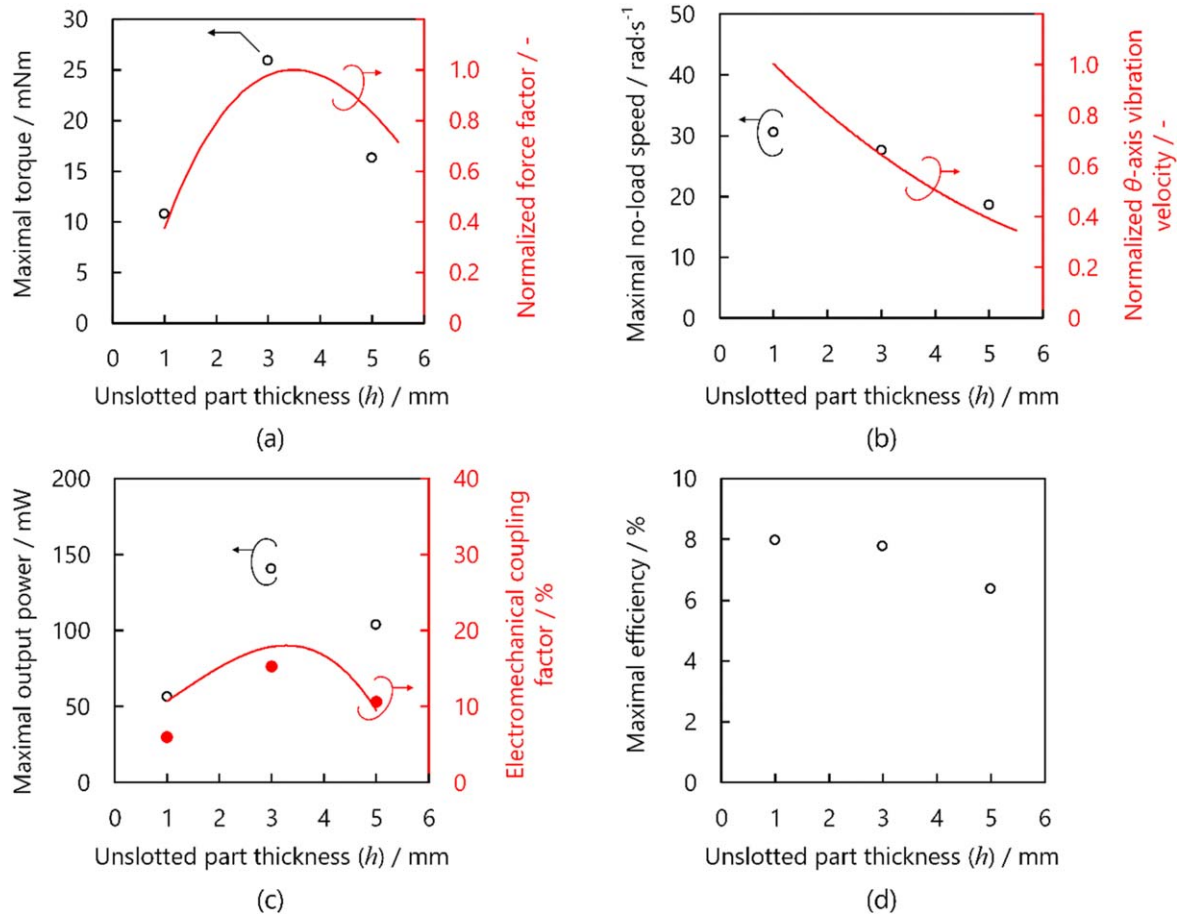


Figure 9. (a) Maximal torque, (b) maximal no-load speed, (c) maximal output power, and (d) maximal efficiency as functions of unslotted part thickness. The solid lines in (a)–(c) are estimated via FEA. The method to calculate electromechanical coupling factors is given in appendix B.

Table 2. Performance comparison between alumina/PZT and stainless-steel/PZT motors.

Performance	Alumina/PZT with h3 vibrator		Stainless-steel/PZT	
	High vibration region	Low vibration region	Low vibration region	High vibration region
Applied voltage/V	20	20	20	250
Electric field intensity in PZT/ $V\text{ mm}^{-1}$	40	40	40	500
Driving frequency/kHz	71.2	26.1	26.1	25.4
Force factor/ $N\text{ V}^{-1}$	0.033	0.014	0.014	
Equivalent damper/ $N\text{ s m}^{-1}$	0.516	2.089	2.089	
Applicable preload/N	6.3	0.8	0.8	13.8
θ -axis vibration velocity/ mm s^{-1}	511	58	58	366
Electromechanical coupling factor	15.3%	4.9%	4.9%	
Maximal torque/mN m	25.9	3.2	3.2	46.8
Maximal rotation speed/ rad s^{-1}	27.7	4.2	4.2	20.8
Maximal output power/mW	141.0	3.8	3.8	351.6
Maximal efficiency	7.8%	1.4%	1.4%	5.6%
Ratio of maximal torque to applied voltage/ mN m V^{-1}	1.3	0.2	0.2	0.2
Ratio of maximal output power to applied voltage/ mW V^{-1}	7.1	0.2	0.2	1.4

stainless-steel/PZT one. On the other hand, the high Young's modulus leads to a relatively high electromechanical coupling factor of the alumina/PZT motor. In the meantime, it has

slightly higher efficiency; these reasons enable the alumina/PZT motor to exhibit a higher maximal-output-power-to-voltage (P-to-U) ratio [1, 8].

4.4. Potential application areas

Recently, robotics and/or precision machines have become increasingly required in the chemical industry [30, 31]. For conventional metal/PZT USMs, shields are required to isolate their metal parts from the acid or alkaline atmosphere to avoid corrosion [30]. It is known that alumina has high chemical resistance [32] (for instance, the weight losses of alumina products with >99.5% purity are respectively <0.07 and <0.05 g cm⁻² per 24 h in HNO₃ and NaOH [30]). As a consequence, our motor can be applied directly to the acid/alkaline environment if its rotor and accessory parts are made of alumina (currently, alumina bearings are commercially available [33] and the rotor can be specially ordered [27]). Another potential application field goes to the intensively alternating-current magnetic field as alumina's high conductive resistance (>10¹⁴ Ω m) [34] may suppress the eddy current and consequently the temperature rise in the vibrator [35]. Here, it would be worthwhile to mention the alumina/PZT motor's expense, averagely 240 dollars for these prototypes. Though it is higher than that of the stainless-steel/PZT one (nearly 40 dollars), in mass production, the expense may be lowered as the mold and/or the machining tool for fabricating alumina vibrating bodies are reusable [36]. To sum up, our motor would be applicable for some special environments owing to alumina's unique property.

5. Conclusions

In this study, we fabricated an alumina/PZT ring-shaped vibrator and employed it to form a traveling-wave USM. Owing to the high Young's modulus and low ultrasonic attenuation, this motor was capable of providing high force factors, high electromechanical coupling factors, and low damping; this partially verified the validity of our proposal. At 20 V, the alumina/PZT motor (h3) yielded the maximal torque, no-load speed, and maximal output power of 25.9 mN m, 27.7 rad s⁻¹, and 141 mW, respectively. Compared to the stainless-steel/PZT motor with similar structure, the alumina/PZT one provided relatively high T-to-U and P-to-U ratios. Besides, the highly chemical resistance and highly conductive resistance may make our motor applicable to several special environments. Through this investigation, we have gained an understanding on alumina/PZT motors and anticipate that these results would provide adequate information for structural optimization in the future.

Acknowledgments

The authors thank the staff members of the Precision and Manufacturing Center, Technical Department, Tokyo Institute of Technology, for machining the motor components. They also thank Mr Yidi Zhou and Dr Jixiao Liu, who are with Hebei University of Technology, for the help in using the microscope. This work was supported by JSPS KAKENHI (Grant Number 17J05057) and National Key Research and Development Plan (Number 2016YFE0128700).

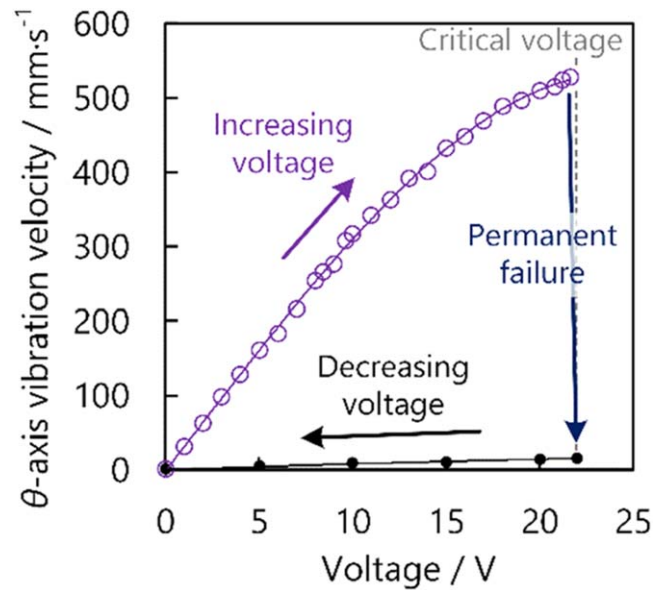


Figure A1. Variation of the θ -axis vibration velocity as functions of applied voltage (0–23 V).

Table A1. Critical voltage and corresponding stress of alumina/PZT vibrators.

Unslotted part thickness (h)/mm	1	3	5
Critical voltage/V	22	22	28
Maximal stress corresponding to critical voltage/MPa	29	23	22

Appendix A. Failure condition

As mentioned in section 3, the vibration velocity of the h3 vibrator is hysteresis-freely dependent on the voltage in the range of 0–20 V (see figure 4). However, when the voltage was increased to 23 V, the vibration velocity sharply decreased from 528 to 15 mm s⁻¹ and did not recover its prior state (see figure A1). The permanent failure also existed on h1 and h5 vibrators (see table A1), while it did not appear on the stainless-steel/PZT vibrator, where the applied voltage reached 250 V.

The reason for the permanent failure was analyzed through FEA. Figure A2(a) illustrates the model and figure A2(b) shows the stress distribution of the h3 vibrator at its critical voltage (22 V). Here, a 50 μm thick epoxy-resin bonding layer, whose Young's modulus, density, and Poisson's ratio are respectively 5.0 GPa, 1.2 × 10³ kg m⁻³, and 0.38 [37, 38], is sandwiched between the alumina vibrating body and the PZT disk. As figure A2(c) illustrates, stress concentration exists on the part of the alumina vibrating body that is in contact with the bonding layer. Besides, the maximal stress reaches 23 MPa, approaching epoxy-resin's shear strength (~25 MPa) [39, 40]. Whereas the maximal stress of the stainless-steel/PZT vibrator is ~12 MPa (see figure A2(d)) despite the applied voltage of 250 V. Previous studies [41, 42] also demonstrate that, for

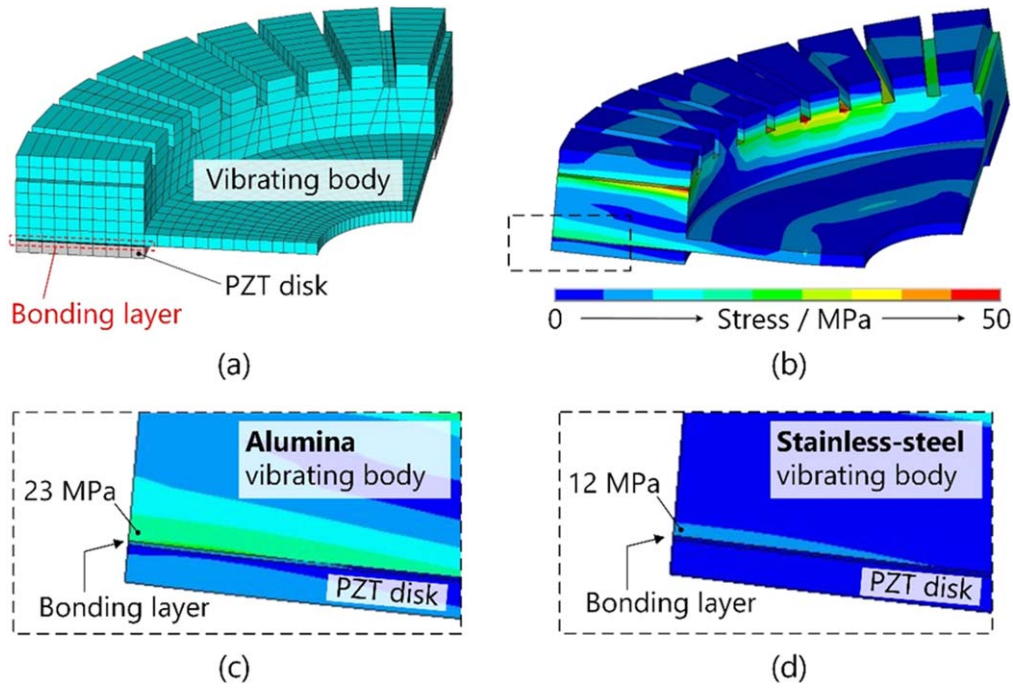


Figure A2. Analysis of stress concentration in vibrators. (a) and (b) are the FEA model and stress distribution of the entire vibrator. (c) and (d) show the stress distributions of the alumina/and stainless-steel/PZT vibrators at 22 and 250 V, respectively.

multilayer composites, stress concentration tends to intensively exist when sandwiched and sandwiching layers have great difference in Young's moduli. Recently, metallic foils have been reported to be utilized as the bonding layers of piezoelectric vibrators [43]; this approach possibly mitigates the above problem as metals generally have higher Young's moduli than epoxy resin [11, 12].

Appendix B. Method of calculating electromechanical coupling factor

The electromechanical coupling factor; which is, in this study, defined as the ratio of mechanical energy to the sum of mechanical and electrical energies stored in the vibrator [44]; is calculated with the following procedures [44]:

- (1) Calculate the vibration velocity distribution through FEA.
- (2) Estimate the vibration energy stored in the vibrator from the above results as [44]

$$U_m = \frac{1}{2}m \cdot \frac{\sum_{i=1}^n (v_{z-i}^2 + v_{\theta-i}^2 + v_{r-i}^2)}{n}, \quad (\text{A1})$$

where m represents the vibrator's mass; v_{z-i} , $v_{\theta-i}$, and v_{r-i} denote vibration velocities of the i th node along the vertical (z), circumferential (θ), and radial (r) directions, respectively; and n is the total number of the model's nodes.

- (3) Calculate the electrical energy as [44, 45]

$$U_e = \frac{1}{2}C_d u^2 = \frac{1}{2} \cdot \frac{\epsilon_{33} S}{t_p} \cdot u^2, \quad (\text{A2})$$

where C_d and u represent the electrical capacitance and the applied voltage, respectively; and ϵ_{33} , S , and t_p denote the permittivity, the electrode's area, and the PZT disk's thickness, respectively.

- (4) Estimate the electromechanical coupling factor with the following equation [45]:

$$k = \sqrt{\frac{U_m}{U_m + U_e}}. \quad (\text{A3})$$

Using this method, we calculated the electromechanical coupling factors of the vibrators whose unslotted parts have varying thickness. As shown in figure 9(c), the alumina/PZT vibrators with thickness of 3–4 mm exhibit higher electromechanical coupling factors probably because of their better acoustic impedance matching than the others [11].

Appendix C. Microscope photos of motors' surfaces

The friction surfaces after intermittent operation of ~ 2 h were observed with a microscope (SMZ-745T, Nikon, Tokyo, Japan). Figures A3(a) and (b) illustrate that aluminum powder, scratched from the rotor, exists on the alumina/PZT vibrators' friction surfaces. Figures A3(c) and (d) illustrate that the severe wear regime on the rotor's surface is

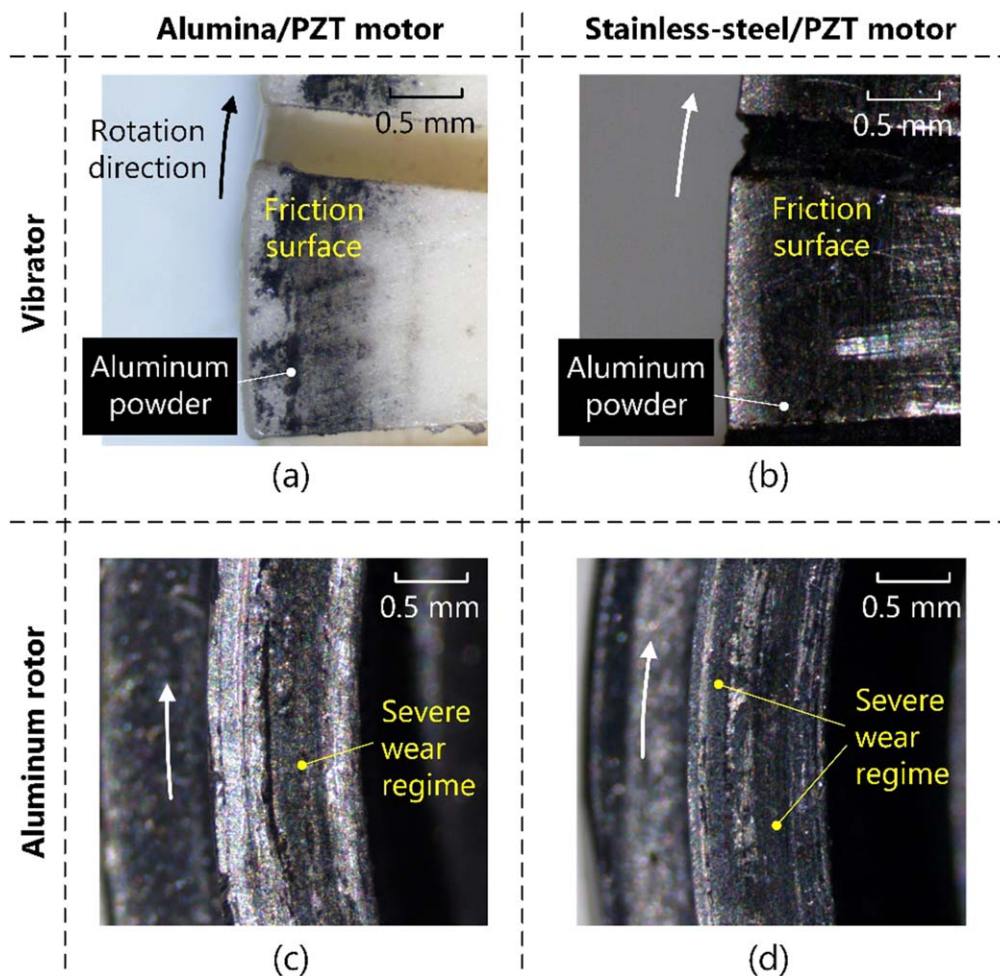


Figure A3. Microscope photos of (a) the alumina/and (b) stainless-steel/PZT vibrators. Those in (c) and (d) are the rotors of the alumina/and stainless-steel/PZT motors.

seemingly smaller for the alumina/ than for the stainless-steel/PZT motor. Though these results may indicate the alumina/PZT motor's high durability [27], we still need to fully prove it by conducting a long-term performance test. Such a long-term life test is left for further studies.

ORCID iDs

Jiang Wu  <https://orcid.org/0000-0002-6899-5601>
 Yosuke Mizuno  <https://orcid.org/0000-0002-3362-4720>
 Kentaro Nakamura  <https://orcid.org/0000-0003-2899-4484>

References

- [1] Ueha S and Tomikawa Y 1993 *Ultrasonic Motors—Theory and Applications* (New York: Oxford University Press) pp 4–13
- [2] Nakamura K, Kurosawa M and Ueha S 1991 Characteristics of hybrid transducer-type ultrasonic motor *IEEE Trans. Ultrason. Ferroelectr. Freq. Control* **38** 188–93
- [3] Pan S, Wu Y, Zhang J, Zhou S and Zhu H 2018 Modeling and control of a 2-degree-of-freedom gyro-stabilized platform driven by ultrasonic motors *J. Intell. Mater. Syst. Struct.* **29** 2324–32
- [4] Wu J, Mizuno Y and Nakamura K 2018 Polymer-based ultrasonic motor utilizing high-order vibration modes *IEEE/ASME Trans. Mechatronics* **23** 788–99
- [5] Zhu Z, To S, Ehmann K F and Zhu X 2017 Design, analysis, and realization of a novel piezoelectrically rotary spatial vibration system for micro/nanomachining *IEEE/ASME Trans. Mechatronics* **22** 1227–37
- [6] Ozeki S, Kurita K, Uehara C, Nakane N, Sato T and Takeuchi S 2018 Analysis of coiled stator ultrasound motor: Fundamental study on analysis of wave propagation on acoustic waveguide for coiled stator *Japan. J. Appl. Phys.* **57** 07LB12
- [7] Zhang Q, Chen W, Liu Y, Liu J and Jiang Q 2017 A frog-shaped linear piezoelectric actuator using first-order longitudinal vibration mode *IEEE Trans. Ind. Electron.* **64** 2188–95
- [8] Zhao C 2011 *Ultrasonic Motors: Technologies and Applications* (Beijing: Science Press) pp 448–68
- [9] Shi S, Huang Z, Yang J, Liu Y, Chen W and Uchino K 2018 Development of a compact ring type MDOF piezoelectric ultrasonic motor for humanoid eyeball orientation system *Sensors Actuators A* **272** 1–10
- [10] Wu J, Mizuno Y, Tabaru M and Nakamura K 2015 Ultrasonic motors with polymer-based vibrators *IEEE Trans. Ultrason. Ferroelectr. Freq. Control* **62** 2169–77

- [11] Wu J, Mizuno Y and Nakamura K 2017 Structural parameter study on polymer-based ultrasonic motor *Smart Mater. Struct.* **26** 115022
- [12] Wu J, Mizuno Y and Nakamura K 2018 Ultrasonic motors with poly phenylene sulfide/alumina/PZT triple-layered vibrators *Sensors Actuators A* **284** 158–64
- [13] Wachtman J B, Cannon W R and Matthewson M J 2009 *Mechanical Properties of Ceramics* 2nd edn (New York: Wiley) pp 89–115
- [14] Rehbein P and Wallaschek J 1998 Friction and wear behavior of polymer/steel and alumina/alumina under high-frequency fretting conditions *Wear* **216** 97–105
- [15] Song J, Liu X, Zhao G, Ding Q and Qiu J 2019 Effect of surface roughness and reciprocating time on the tribological properties of the polyimide composites *Polym. Eng. Sci.* **59** 483–9
- [16] Wang L, Hofmann V, Bai F, Jin J and Twiefel J 2018 Modeling of coupled longitudinal and bending vibrations in a sandwich type piezoelectric transducer utilizing the transfer matrix method *Mech. Syst. Signal Process.* **108** 216–37
- [17] Zhao G, Wu C, Zhang L, Song J and Ding Q 2018 Friction and wear behavior of PI and PTFE composites for ultrasonic motors *Polym. Adv. Technol.* **29** 1487–96
- [18] Liu Y, Yan J, Wang L and Chen W 2019 A two-DOF ultrasonic motor using a longitudinal-bending hybrid sandwich transducer *IEEE Trans. Ind. Electron.* **66** 3041–50
- [19] Aoyagi M, Beeby S P and White N M 2002 A novel multi-degree-of-freedom thick-film ultrasonic motor *IEEE Trans. Ultrason. Ferroelect. Freq. Control* **49** 151–8
- [20] Wang L, Shu C, Jin J and Zhang J 2017 A novel traveling wave piezoelectric actuated tracked mobile robot utilizing friction effect *Smart Mater. Struct.* **26** 035003
- [21] Li X and Zhou S 2016 A novel piezoelectric actuator with a screw-coupled stator and rotor for driving an aperture *Smart Mater. Struct.* **25** 035027
- [22] Liu Y, Shi S, Li C, Chen W, Wang L and Liu J 2018 Development of a bi-directional standing wave linear piezoelectric actuator with four driving feet *Ultrasonics* **84** 81–6
- [23] Li X and Yao Z 2016 Analytical modeling and experimental validation of a V-shape piezoelectric ultrasonic transducer *Smart Mater. Struct.* **25** 075026
- [25] Kurosawa M and Ueha S 1988 Efficiency of ultrasonic motor using traveling wave *J. Acoust. Soc. Japan.* **44** 40–6 (In Japanese)
- [26] Alumina ceramic products (<http://ceratech.co.jp/product/material/alumina>) [Accessed: 22 Oct. 2019]
- [27] Qiu W, Mizuno Y and Nakamura K 2016 Tribological performance of ceramics in lubricated ultrasonic motors *Wear* **352/353** 188–95
- [28] Hirata H and Ueha S 1992 Force factor design of disk vibrators used for ultrasonic motors *J. Acoust. Soc. Japan E* **13** 77–84
- [29] Santos A, Cordoba E, Ramirez Z, Sierra C and Ortega Y 2017 Determination of the coefficient of dynamic friction between coating of alumina and metallic materials *IOP J. Phys.: Conf. Ser.* **935** 012042
- [30] Zheng L, Liu S and Wang S Current situation and future of Chinese industrial robot development *Int. J. Mech. Eng. Robot. Res.* **5** 295–300
- [31] Nishioka H and Takeuchi A 2018 The development of high technology industry in Japan *The Development of High Technology Industries—An International Survey* (New York: : Routledge, Taylor and Francis Group) pp 265–8
- [32] Richerson D W 2006 *Modern Ceramic Engineering—Properties, Processing, and Use in Design* (New York: USA: Taylor and Francis Group) pp 573–9
- [33] Davis J R 2000 *Corrosion: Understanding the Basics* (Materials Park: ASM International) pp 295–7
- [34] Kyocera fine ceramics (<https://kyocera.co.jp/prdct/fc/product/pdf/material.pdf>) [Accessed: 22 Oct 2019]
- [35] Mason W P 1956 Physical acoustics and the properties of solids *J. Acoust. Soc. Am.* **28** 1197–206
- [36] Bengisu M 2001 *Engineering Ceramics* (New York: Springer) pp 85–102
- [37] Jin F-L, Li X and Park S-J 2015 Synthesis and application of epoxy resins: a review *J. Ind. Eng. Chem.* **29** 1–11
- [38] Wu C and Xu W 2006 Atomistic molecular modelling of crosslinked epoxy resin *Polymer* **47** 6004–9
- [39] Epoxy adhesive application guide (http://epotek.com/site/files/brochures/pdfs/adhesive_application_guide.pdf) [Accessed: 22 Oct. 2019]
- [40] Technical data sheet of Henkel's epoxy-resin adhesive (http://loctiteproducts.com/tds/EPXY_QSET_S_tds.pdf) [Accessed: 22 Oct. 2019]
- [41] Mousa S and Kim G-Y 2015 Experimental study on warm roll bonding of metal/polymer/metal multilayer composites *J. Mater. Process. Technol.* **222** 84–90
- [42] Jafari M and Ardalani E 2016 Stress concentration in finite metallic plates with regular holes *Int. J. Mech. Sci.* **106** 220–30
- [43] Nicolay P, Bardong J, Chambon H and Dufilie P 2018 Glue-less and robust assembly method for SAW strain sensors *Proc. 2018 IEEE Int. Ultrasonics Symp.*
- [44] Wu J, Mizuno Y and Nakamura K 2019 Piezoelectric motor utilizing an alumina/PZT transducer *IEEE Trans. Ind. Electron.* (<https://doi.org/10.1109/TIE.2019.2937047>)
- [45] Morita T 2017 *Piezoelectric Phenomena* (Tokyo: Morikita Publication) pp 36–9 (In Japanese)